A Compressive-Sensing Approach for Opportunistic Bistatic SAR Imaging Enhancement by Harnessing Sparse Multiaperture Data

Adrian Focsa, *Student Member, IEEE*, Andrei Anghel, *Senior Member, IEEE*, and Mihai Datcu, *Fellow, IEEE*

***Abstract*— This article introduces a compressive sensing (CS)-based approach for increasing bistatic synthetic aperture radar (SAR) imaging quality in the context of a multiaperture acquisition. The analyzed data were recorded over an opportunistic bistatic setup including a stationary ground-based-receiver opportunistic C-band bistatic SAR differential interferometry (COBIS) and Sentinel-1 C-band transmitter. Since the terrain observation by progressive scans (TOPS) mode is operated, the receiver can record synchronization pulses and echoed signals from the scene during many apertures. Hence, it is possible to improve the azimuth resolution by exploiting the multiaperture data. The recorded data are not contiguous and a naive integration of the chopped azimuth phase history would generate undesired grating lobes. The proposed processing scheme exploits the natural sparsity characterizing the illuminated scene. For azimuth profiles recovery greedy, convex, and nonconvex CS solvers are analyzed. The sparsifying basis/dictionary is constructed using the synthetically generated azimuth chirp derived considering Sentinel-1 orbital parameters and COBIS position. The chirped-based CS performance is further put in contrast with a Fourier-based CS method and an autoregressive model for signal reconstruction in terms of scene extent limitations and phase restoration efficiency. Furthermore, the analysis of different receiver-looking scenarios conducted to the insertion in the processing chain of a direct and an inverse Keystone transform for range cell migration (RCM) correction to cope with squinted geometries. We provide an extensive set of simulated and real-world results that prove the proposed workflow is efficient both in improving the azimuth resolution and in mitigating the sidelobes.**

***Index Terms*— Bistatic, compressive sensing (CS), multiaperture, opportunistic acquisition.**

Manuscript received November 5, 2020; revised February 18, 2021; accepted April 3, 2021. This work was supported in part by the European Space Agency (ESA) through the TomoSAR-1B Project under Contract 4000124573/18/NL/CBi. *(Corresponding author: Andrei Anghel.)*

Adrian Focsa is with the Research Center for Spatial Information, University Politehnica of Bucharest, 060032 Bucharest, Romania, and also with Military Technical Academy "Ferdinand I", 050141 Bucharest, Romania (e-mail: focsa.adrian@yahoo.com).

Andrei Anghel is with the Department of Telecommunications, Research Center for Spatial Information, University Politehnica of Bucharest, 060032 Bucharest, Romania (e-mail: andrei.anghel@munde.pub.ro).

Mihai Datcu is with the German Aerospace Center, 82234 Weßling, Germany, and also with the Research Center for Spatial Information, University Politehnica of Bucharest, 060032 Bucharest, Romania (e-mail: mihai.datcu@dlr.de).

Color versions of one or more figures in this article are available at https://doi.org/10.1109/TGRS.2021.3071861.

Digital Object Identifier 10.1109/TGRS.2021.3071861

I. Introduction

BISTATIC Synthetic Aperture Radar (Bi-SAR) [1], [2] imaging provide a list of advantages as compared to monostatic acquisition setups. Complementary information encapsulated in the bistatic data is often exploited in applications such as automatic target recognition, scene classification, and SAR interferometric measurements. Lately, the particular case of space-borne transmitter-ground-based stationary receiver emerged [3]–[5], [6]. A significant drawback is that most of the bistatic systems have a degraded cross-range resolution as compared to the monostatic systems. Even so, multiaperture data availability leads to the improvement of bistatic imaging [6], [7].

Many opportunistic bistatic SAR systems were developed. Different synchronization aspects were evaluated depending on the employed SAR image focusing procedure and the transmitter scanning mode. In [8], the stationary C-band receiver a SAR bistatic receiver for interferometric applications (SABRINA) used ERS2 and ENVIronment SATellite (ENVISAT) as transmitters operating in stripmap mode. The phase synchronization together with Doppler Centroid estimation was achieved using a Tx-Rx direct path signal recorded using a dedicated channel. Several bistatic experiments using the German satellite TerraSAR-X as a transmitter of opportunity were conducted. The HITCHHIKER receiver [4] in sliding-spotlight mode, the stationary platform in [9] in staring-spotlight mode, and also the airborne/space-borne system phased array multifunctional imaging radar (PAMIR) [10], trigger the acquisition using the reference channel signal. As in [4], the time-frequency synchronization of opportunistic C-band bistatic SAR differential interferometry (COBIS) [5] platform is achieved by exploiting the frequency reference and the timestamps provided by a global positioning system (GPS) disciplined local oscillator (LO). COBIS is also a multichannel ground-based receiver that uses Sentinel-1 as a transmitter of opportunity operating in terrain observation by progressive scans (TOPS) mode [11]. It comprises a direct path channel and three imaging channels with up to 200 MHz instantaneous bandwidth. It provides the data in the experiments presented in this article. The received data alignment is performed by linking the ground-based platform receiving timestamps with the transmission timestamps provided in the Sentinel-1 A/B ancillary data.

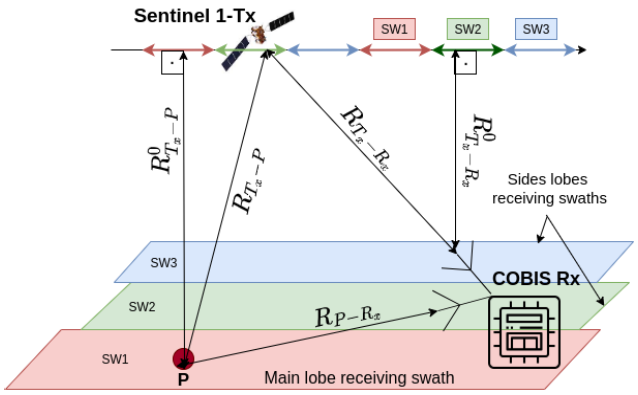

Fig. 1. Simplified acquisition geometry-bistatic SAR. The multiple subswaths (SW1, SW2, SW3) intervals are sketched on the transmitter (Sentinel-1) path using consecutive RGB double arrow segments. Also, the Tx-Rx relative distances of a point P in the illuminated area are displayed.

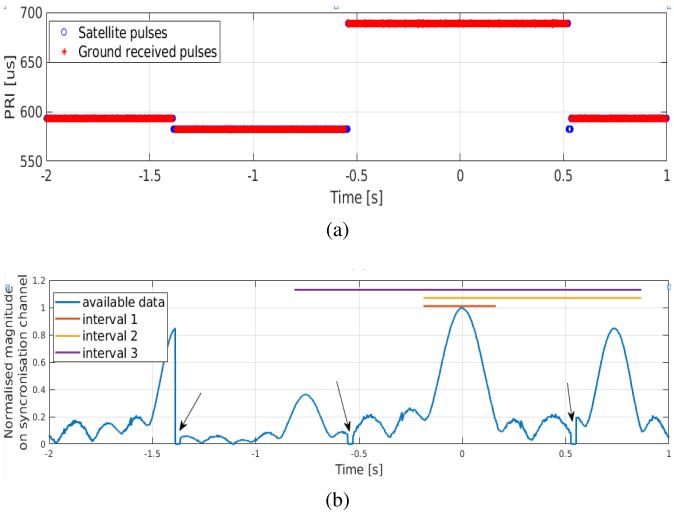

Fig. 2. (a) Example of direct path PRI. (b) Normalized magnitude on synchronization channel. The black arrows indicate the severely low SNR acquisition windows.

In this way, each received pulse is linked to the transmission and hence the satellite position is determined. To eliminate the unknown phase difference between the satellite's LO and the ground receiver's LO the range compression processing uses the synchronization channel signal. Since terrain observation with progressive scans SAR (TOPSAR) mode [11] is operated over the area where the receiver is disposed, multiple bursts (see Fig. 2) may be employed for SAR processing [12].

In the last decade, compressive sensing (CS) techniques [13], [14] have been extensively used in signal processing applications and recently integrated in classifications problems, [15]. Specifically, in the context of remote sensing, many improvements have been achieved by posing problems in the framework of CS. For transposing the SAR image generation in terms of CS theory most of the approaches use the acquisition model to derive the dictionary considering raw SAR data as representing the Fourier k-space measurements of the spatial reflectivity field [16], [17]. Often, to treat the 2-D data in such a large-scale problem, azimuth and range reconstructions are decoupled [18]. Even so, in many cases, a range cell migration correction (RCMC) should be taken into consideration. Commonly, RCMC is performed in the range-Doppler domain as is the case of Range Doppler Algorithm for SAR focusing [19], thanks to its property of ensuring the target azimuth position invariance. In Chirp Scaling Algorithm [20], [21], the range walk compensation is achieved in the time domain by multiplying the raw data (before range compression) with a phase compensation term. However, the Keystone transform (KT) [22] performed in the $\omega - \eta$ (range frequency-azimuth time) domain may accomplish the correction of the linear migration by range-dependent azimuth interpolation. KT has been successfully employed in both SAR [23], inverse SAR, or moving target indication applications [24]. More advanced versions of KT, Generalized KT [25] and segmented KT [26] were developed for addressing high order polynomial approximation of the nonlinear RCM problem.

In this article, we propose a processing framework for opportunistic bistatic SAR imaging where the resolution enhancement is achieved from multiaperture processing. The sparse data from multiple apertures are available as a result of the TOPSAR scanning mode. As displayed in Fig. 2(b), the multiaperture data may come from both Tx sidelobes and side-sections in the main lobe when the Tx antenna is oriented to the other two subswaths (the first and the last bursts in the aperture interval 3). Furthermore, as displayed in Fig. 2(a), the extended aperture involves time subintervals having different pulse repetition intervals (PRI). Thus, the proposed processing accounts for this particularity by resampling the raw data on cross-range direction to a uniform azimuth sampling frequency of 2 kHz.

The contribution of the sidelobes should be carefully introduced in the SAR image formation proportionally to SNR. We choose to employ a CS framework to solve this problem. First, the range compressed bistatic signal obtained using a receiver dedicated synchronization channel is characterized by an extremely low azimuth bandwidth rate, conducting to a Fourier oriented workflow. However, for large azimuth integration intervals, the narrow-band assumption cannot be employed anymore. That is why we have introduced a reramping processing step to restore the semimonostatic phase. Furthermore, a chirp-based dictionary replaces the Fourier basis in the CS frame. Moreover, our framework takes into account the particularities for RCM of such an opportunistic acquisition. As derived in Section II, the range dependent cell walk is handled by the KT. We perform the validation on two special cases of space-borne transmitter stationary ground-based receiver acquisition scenarios. The first considers the case in which the receiver and the transmitter line-of-sight (LOS) vectors projections onto a planar approximation of the Geo-referenced focusing grid are approximately collinear. In the second case, the nonorthogonality of the two projections is considered. Consequently, the range-walk is significantly higher than in the first scenario and it should be compensated before azimuth profiles processing. Since the high-order components of the RCM trajectory may be neglected, the KT is applied to perform the correction. Lastly, the range-compressed recovered data is focused through back-projection (BP) algorithm [27].

The remainder of this article is organized as follows. In Section II the bistatic signal model along with the RCMC

are discussed whereas in Section III the theory of CS is briefly reviewed highlighting the particularities of the multiaperture reconstruction. Besides, relevant CS solvers are discussed. The proposed processing workflow is detailed in Section IV. Finally, the results on both simulations and real-world data are illustrated and discussed in Section V. Section VI presents the conclusions of this article.

II. Bistatic Signal Model

The bistatic acquisition scenario relies on the C-band Sentinel-1 transmitter of opportunity and the COBIS ground-based receiver [5]. As illustrated in Fig. 1, the receiver comprises at least two distinct receiving channels. One is oriented toward the satellite (synchronization channel) whereas the other ones are oriented toward the scene of interest.

We consider the transmitted signal, i.e., a linear frequency modulated set of pulses (1) spanning a bandwidth B, in the interval $[F_c-B/2, F_c+B/2]$. The variables τ and η denote the fast time and the slow time, respectively. In (1), K_r denotes the frequency modulation slope, j is the imaginary unit whereas $\mathrm{rect}(\tau/T_0)$ is the rectangular function centered in the origin of the time axis and having the duration T_0

$$s(\tau) = \mathrm{rect}\left(\frac{\tau}{T_0}\right) \times \exp\left[2\pi j\left(-\frac{B}{2}\tau + K_r\frac{\tau^2}{2}\right)\right] \times \exp(2\pi j F_c \tau). \quad (1)$$

In the following, we consider the bistatic processing of a point scatterer P (see Fig. 1). The receiver direct path signal and the echo channel are presented in (2)

$$\begin{aligned} s_{Rx}^{\mathrm{sync}}(\tau,\eta) &= s\left(\tau - \frac{R_{T_x-R_x}(\eta)}{c_0}\right) \\ s_{Rx}^{\mathrm{echo}}(\tau,\eta) &= s\left(\tau - \frac{R_P(\eta)}{c_0}\right) \\ &= s\left(\tau - \frac{R_{T_x-P}(\eta) + R_{P-R_x}(\eta)}{c_0}\right). \end{aligned} \quad (2)$$

The range compression in (3) is performed by employing the synchronization channel as reference

$$\begin{aligned} s_{rc}(\tau,\eta) &= s_{Rx}^{\mathrm{sync}} \otimes s_{Rx}^{\mathrm{echo}} \\ &= A(\tau,\eta) \times \mathrm{MFR}\left(\tau - \frac{R_P^*(\eta)}{c_0}, \eta\right). \end{aligned} \quad (3)$$

In (3), R_P^* denotes an equivalent range history of the target P that will be discussed in Section II-A, "$\otimes$" denotes the cross correlation operation and $A(\tau,\eta)$ models the effect of the antenna azimuth pattern (AAP), the radar cross section of the target and the triangular weighting function resulted from the cross correlation of the linear frequency modulated pulses envelopes. Since the second part is unknown, only the AAP will be taken into account in our bistatic SAR processor. MRF is the matched filter response on the range direction. F_c denotes the carrier frequency.

A. KT-Based RCMC

Any processing applied in the azimuth direction should be performed only if the RCM has been previously corrected. In our case, the stationary target P has a range walk which depends on its relative position to the space-borne transmitter and ground-based receiver. Next, we will derive the RCM for the following particularities of the bistatic acquisition setup: stationary receiver, the distance from the imaging area to Rx is much smaller than to the Tx. The semimonostatic component of the range variation $R_{T_x-P}(\eta)$ is depicted by (4)

$$R_{T_x-P}(\eta) = \sqrt{\left(R_{T_x-P}^0\right)^2 + (V_{\mathrm{sat}}\eta)^2}. \quad (4)$$

Since the processed azimuth time covers many apertures, the second-order approximation of the Taylor expansion in (5) is no longer valid for the semimonostatic phase history

$$\begin{aligned} R_{T_x-P}(\eta) &= R_{T_x-P}^0 + \sum_{k=1}^{\infty} \gamma_k^{\mathrm{echo}} \eta^k \\ R_{T_x-R_x}(\eta) &= R_{T_x-R_x}^0 + \sum_{k=1}^{\infty} \gamma_k^{\mathrm{sync}} \eta^k. \end{aligned} \quad (5)$$

However, because the range compression operator uses a signal which has a similar range azimuth coupling as the one from the echo channel, the high order terms may be neglected for $s_{rc}(\tau,\eta)$. Also, the previously mentioned equivalent range history is given by (6)

$$R_P^*(\eta) = R_{T_x-P}(\eta) + R_{P-R_x} - R_{T_x-R_x}(\eta). \quad (6)$$

By introducing (5) in (6) the following linear approximation of the equivalent bistatic range variation is obtained (7):

$$\begin{aligned} R_P^*(\eta) &= R_{T_x-P}^0 + R_{P-R_x} - R_{T_x-R_x}^0 + \left(\gamma_1^{\mathrm{sync}} - \gamma_1^{\mathrm{echo}}\right)\eta \\ &= R_P^0 + \gamma_{\mathrm{rez}}\eta. \end{aligned} \quad (7)$$

As a consequence of the linear approximation in (7), the azimuth bandwidth is extremely narrow. Therefore, the SAR image may be simply obtained by projecting range compressed data along cross-range dimension in the Fourier domain. This property of azimuth compression through fast Fourier transform (FFT) basis along with the assumption of scene spatial sparsity justifies the possibility of the azimuth profile recovery by CS with Fourier sparsifying dictionary.

From (7), it may be seen that the longer the multiaperture interval, the higher the range walk effect. Since we aim to process each iso-range profile with CS, an RCMC step is necessary.

Furthermore, the RCMC is performed by KT. The range compressed data are Fourier transformed over the range direction. Its analytic form, $S(f,\eta)$ in (8), is derived using the stationary phase approximation

$$S(f,\eta) = A(f,\eta) \times \exp\left[-4\pi j\frac{R_P^*(\eta)}{c_0}(f+F_c)\right]. \quad (8)$$

By introducing (7) into (8), we get

$$S(f,\eta) \approx A(f,\eta) \times \exp\left[-4\pi j\frac{R_P^0}{c_0}(f+F_c)\right] \times \exp\left[-4\pi j\frac{\gamma_{\mathrm{rez}}\eta}{c_0}(f+F_c)\right]. \quad (9)$$

The second exponential term in (9) illustrates the coupling between range and azimuth

$$\eta_m = \frac{F_c}{f+F_c}\eta. \quad (10)$$

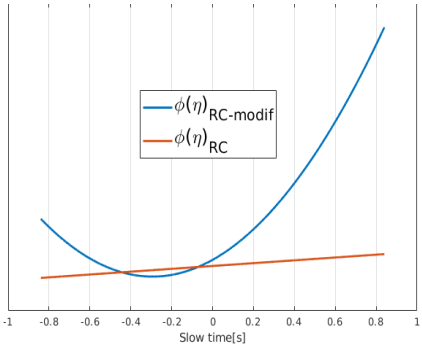

Fig. 3. Range compressed phase history versus reramped phase of a point-like scatterer.

The range-azimuth linear coupling is canceled on the modified azimuth time axis η_m by rescaling the azimuth time η with the range frequency-dependent term in (10). A similar transform is employed for reversing the process. The scaling factor is modified to $((f + F_c)/F_c)$. The main advantage of this RCMC technique is that it works with no prior information about the range migration slope.

B. Azimuth Reramping

The Fourier-based sparsity assumption on the azimuth direction discussed in Section II-A is limited to small integration intervals. Thus, a more robust approach should be considered. In Fig. 3, the simulated unwrapped phase history (after range compression—RC) of a point scatterer validates the assumption of extremely narrow azimuth bandwidth ($\phi_{\text{RC}}(\eta)$) employed in [7] and consolidates the proposed methodology given the expanded bandwidth associated with the blue parabola ($\phi_{\text{RC-modif}}(\eta)$) in Fig. 3. The latter is obtained using the synchronization channel phase history. Both phase histories are defined in (13)

$$\begin{aligned} y_{\text{P-RC}}(\eta) = Z(\eta) \exp\left(-2\pi j F_c \frac{R_{T_x-P}(\eta)}{c_0}\right) \\ \times \exp\left(-2\pi j F_c \frac{R_{R_x-P}}{c_0}\right) \\ \times \exp\left(+2\pi j F_c \frac{R_{T_x-R_x}(\eta)}{c_0}\right). \end{aligned} \tag{11}$$

The azimuth profile of a scatterer P in the scene, $y_{\text{P-RC}}(\eta)$ is given in (11) whereas the modified complex valued profile $y_{\text{P-RC}_{\text{modified}}}(\eta)$ is defined in (12). $Z(\eta)$ accounts for the effects of the azimuth antenna pattern and the variation of the scatterer's radar cross section in slow time. By reducing the phase term corresponding to the time-varying distance between the transmitter and the stationary receiver, we obtain the modified phase history (12) or the reramped azimuth phase

$$\begin{aligned} y_{\text{P-RC}_{\text{modif}}}(\eta) = Z(\eta) \exp\left(-2\pi j F_c \frac{R_{T_x-P}(\eta)}{c_0}\right) \\ \times \exp\left(-2\pi j F_c \frac{R_{R_x-P}(\eta)}{c_0}\right). \end{aligned} \tag{12}$$

In (12), the term $R_{R_x-P}(\eta)$ is a constant, thus the azimuth phase history variation is given only by $R_{T_x-P}(\eta)$

$$\begin{aligned} \phi_{\text{P-RC}}(\eta) &= \angle(y_{\text{P-RC}}(\eta)) \\ \phi_{\text{P-RC}_{\text{modif}}}(\eta) &= \angle(y_{\text{P-RC}_{\text{modif}}}(\eta)). \end{aligned} \tag{13}$$

Since this distance variability is considered only one way (not two way as in monostatic), the resulted cross-range resolution is usually half that in the monostatic case. However, by considering more than one aperture for focusing, the resolution would be remarkably improved. In real-world contexts, the signal from many apertures is received either from the transmitter sidelobes or from side sections on the main lobe for multiswath scanning modes. The latter case occurs when a multiswath scanning mode is employed (e.g., TOPSAR and ScanSAR). Thus, the entire azimuth response of a target looks "chopped" and also contains subintervals with low SNR. Consequently, a recovery/enhancement algorithm should be applied before azimuth focusing. Otherwise, unwanted grating lobes will affect the final SAR image.

III. Compressive-Sensing Reconstruction

A. CS General Framework

The theory of CS [14] guarantees the perfect reconstruction of the original signal $\boldsymbol{x}$ from less samples than the lower bound established by the Nyquist sampling theorem. The classic model of CS is depicted by (14). In (14), $\boldsymbol{\Phi} \in \mathbb{C}^{n\times p}$ denotes the measurement matrix,$\boldsymbol{\Psi} \in \mathbb{C}^{n\times n}$ is the over-complete sparsifying basis, $\boldsymbol{x} \in \mathbb{C}^n$ and $\boldsymbol{y} \in \mathbb{C}^p$ represents the original signal and the available samples, with $p < n$ whereas $\boldsymbol{\epsilon} \in \mathbb{C}^p$ is a vector modeling the noise

$$\boldsymbol{y} = \boldsymbol{\Phi}\boldsymbol{\Psi}\boldsymbol{\alpha} + \boldsymbol{\epsilon} = \boldsymbol{\Theta}\boldsymbol{\alpha} + \boldsymbol{\epsilon}. \tag{14}$$

The sparse representation of $\boldsymbol{x}$ is depicted in (15)

$$\boldsymbol{x} = \boldsymbol{\Psi}\boldsymbol{\alpha}, \quad ||\boldsymbol{\alpha}||_0 = K. \tag{15}$$

In (15), K denotes the sparsity degree and formally is depicted by L_0 norm (cardinality of nonnull coordinates subset of $\boldsymbol{\alpha}$).

The problem of recovering $\boldsymbol{x}$ starts with solving (16) and then replacing the outcome into (15)

$$\min_{\alpha} \|\boldsymbol{y} - \boldsymbol{\Theta}\boldsymbol{\alpha}\|_2^2, \quad \text{s.t. } \|\boldsymbol{\alpha}\|_0 = K. \tag{16}$$

The recovery of the original signal $\boldsymbol{x}$ is guaranteed if $\boldsymbol{\Theta}$ satisfies the Restricted Isometry Property (RIP) and the Mutual Coherency Property (MCP) [13], [28]. Nevertheless, the recovery algorithms impose various lower bounds regarding the sufficient number of measurements relative to the worst cases of RIP and MCP [29], [30].

The opportunistic bistatic multiaperture scenario provides an intermittent extended azimuth response of the scene. To benefit from this feature, without degrading SAR image quality, the useful samples i.e., $\boldsymbol{y}$ (characterized by high SNR) should be involved in the prediction of the missing samples. Thus, by assuming the natural spatial scene sparsity, the answer for this problem may be provided by the CS tools.

B. CS Solvers Overview

The L_0 constraint makes the CS problem NP-hard. Thus, many CS solvers emerged based on its convex relaxation L_1 (least absolute shrinkage and selection operator (LASSO) [31], Dantzig Selector [32], Basis Pursuit and, Basis Pursuit

Denoising [33]). Typically, to solve such problems either greedy algorithms or convex/nonconvex relaxations may be employed. Out of the first category, orthogonal matching pursuit (OMP) [34], regularized OMP (ROMP) [35], generalized OMP (GOMP) [36], CoSaMP [37], iterative hard thresholding (IHT) [38], subspace pursuit (SP) [39], conjugate gradient iterative hard thresholding (CGIHT) [40], hard thresholding pursuit (HTP) [41], SWAP [42], and correntropy matching pursuit (CMP) [43] will be further discussed. In the category of convex relaxed approaches, Approximate Message Passing (AMP) [44], SPGL1-BPDN [45], and fast iterative shrinkage-thresholding algorithm (FISTA) [46] algorithms are evaluated. Finally, the BCS algorithm [47], Iterative Reweighted Least Squares (IRLS) [48], and Iterative Jumping Threshold (IJT) [49] with $L_{2/3}$ penalty are considered representatives for nonconvex relaxation-based CS solvers.

1) Greedy Solvers: The main idea of the greedy algorithms is to iteratively select the dictionary atoms having the best correlation coefficients. The main differences between them are the number of dictionary atoms kept at each iteration and the moment when the solution (usually a least square estimate) is computed (at each iteration or in the end). ROMP [35] and GOMP [36] are advanced alternatives for OMP which provide better reconstructions either by using a regularization step or by updating the support vector set with multiple atoms. In contrast to OMP, some of the atoms selected at one iteration may be dismissed until the final result is computed. Most of the greedy algorithms use the degree of correlation between the residual and the basis vectors to select the candidates from the sparsifying dictionary and the final solution is computed as a least-squares (LS) estimate of the underdetermined system. CoSaMP [37] first identifies the atoms that have the greatest degree of similarity with the residual and then updates the support set with the newly found vectors. Then an intermediate LS solution is computed. At this point, the pruning step is applied. Thus, only the largest coefficients from the solution are retained and finally, the LS solution is reevaluated. The main differences between SP [39] and CoSaMP are related to the number of selected atoms (SP is less complex than CoSaMP) and the threshold used in the pruning step. Since both CoSaMP and SP select multiple dictionary vectors, they are considered parallel greedy algorithms. CoSaMP/SP are not suitable for CS frameworks with low-rank measurement matrix as is the case of narrow-band azimuth signal recovery using chirp-based sensing matrix. IHT algorithm is an iterative algorithm introduced in [38]. It encourages the biggest coefficients obtained at each step by using the hard-thresholding nonlinear function. The intermediate solution is achieved using (17)

$$\tilde{\boldsymbol{x}}_{t+1} = \mathcal{S}\big(\tilde{\boldsymbol{x}}_t + \lambda \boldsymbol{\Theta}^H(\boldsymbol{y} - \boldsymbol{\Theta}\tilde{\boldsymbol{x}}_t)\big). \tag{17}$$

In (17), $\mathcal{S}$ denotes the shrinkage operator whereas λ accounts for the amount of change at each iteration and $(.)^H$ denotes the Hermitian transpose operator. IHT is less computational demanding than other nonconvex solvers (e.g., IRLS [48], IRL1 [50]), therefore IHT is suitable for large scale problems. HTP [41] and its variants fast hard thresholding pursuit (FHTP) and normalized hard thresholding pursuit (NHTP) combine ideas from both CoSaMP and IHT. SWAP algorithm proposed in [42] is a greedy solver that should be provided either an initial set of support vectors or a simple and fast algorithm (e.g., OMP) to generate the initial guess. On each iteration, the support set is modified in such a way a cost function is optimized. Hence, SWAP offers a good solution to the L_0 constrained problem even if the atoms in the measurement matrix are correlated. However, SWAP has a higher computational complexity than the other greedy solvers because of its "brute-force"/combinatorial manner of reaching the solution. Correntropy Matching Pursuit (CMP) was recently introduced in [43]. CMP replaces the mean square error by the correntropy cost function. In this way, the effect of the outliers is mitigated and also accounts for the false Gaussianity assumption on the errors.

2) Nonconvex Relaxation Solvers: The inversion problem of CS may be also solved by transposing it in terms of Bayesian formalism, as in BCS [47]. The basic idea of the IRLS algorithm [48] is to obtain an approximate sparse solution by solving an ensemble of weighted least squares problems. Each basis vector is assigned a weight and each iteration the weights are adjusted. Finally, the solution is computed via (18), where $\boldsymbol{Q}$ is a diagonal matrix containing the weights

$$\tilde{\boldsymbol{x}} = \boldsymbol{Q}\boldsymbol{\Theta}^H(\boldsymbol{\Theta}\boldsymbol{Q}\boldsymbol{\Theta}^{\boldsymbol{H}})^{-1}\boldsymbol{y}. \tag{18}$$

IJT [49] employs a sub unitary norm Lq, $(0 < q < 1)$ as nonconvex penalty. Innovative jump discontinuous thresholding functions are also used in IJT. Even though they are more difficult to solve than the nonconvex penalties, subunitary norm constrain forces the solution to be sparser than the convex regularization constraints based on L_1 norm.

3) Convex Relaxation Solvers: AMP is an iterative thresholding algorithm proposed in [44], which aims to reduce the lower bound of sparsity-undersampling ratio for which the reconstruction is guaranteed. It provides qualitative results on a CS framework involving structured sensing dictionaries (Fourier, circulant matrices, and Toeplitz). SPGL1-BPDN [45] offers a fast convergence and an accurate estimate under high SNR conditions. FISTA [46] is a version of ISTA [51] in which the low convergence rate specific to this category of solvers is improved.

The greedy algorithms are preferred instead of the convex/nonconvex approaches due to their fast convergence. Yet, their major disadvantage is related to the sparsity degree estimation. The overestimation of K leads to the failure of the reconstruction. IRLS, AMP, SPGL1, and FISTA provide proper results under low to mild noise conditions ($SNR > 0[dB]$). IRLS proves the least robustness to noise. By contrast, most of the greedy algorithms succeed in recovering a signal similar to an azimuth profile depicted by (12) as long as the lowest nonzero element in $\boldsymbol{\alpha}$ exceeds the noise power [52].

C. Proposed Sparsifying Dictionary

The proposed framework stands on the idea of a chirp-based sparsifying dictionary i.e., $\boldsymbol{\Psi}^{\text{CHIRP}}$. Yet, for comparison, the processing flow is also adapted for the Fourier basis i.e., $\boldsymbol{\Psi}^{\text{FFT}}$. Both complex-valued basis satisfy the RIP and the MCP [13]. The atoms in $\boldsymbol{\Psi}^{\text{CHIRP}}$ are constructed using the transmitter orbital information (position, velocity and, acceleration) and a reference point (usually mid-scene position). First, the reference phase history $\boldsymbol{\Psi}_{\text{ref}}^{\text{CHIRP}}$ is computed. Then, each

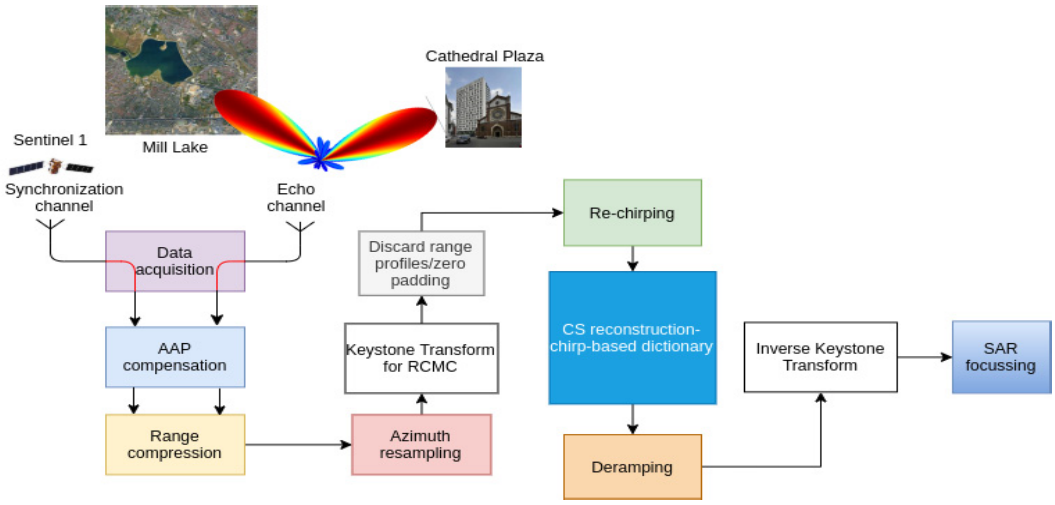

Fig. 4. Sparse multiaperture reconstruction framework: CS-CHIRP.

dictionary atom Ψ_i^{CHIRP} is obtained using (19). In (19), PRF refers to pulse repetition frequency whereas η_{aperture} denotes the considered aperture time interval, λ is the wavelength whereas *rect()* represents the boxcar function (zero-centered) having the impulse width equal to the denominator of its argument

$$\begin{aligned}\Psi_i^{\text{CHIRP}} &= \Psi_{\text{ref}}^{\text{CHIRP}}\left(\eta - i\frac{1}{PRF}\right)\\ &= \text{rect}\left(\frac{\eta - i\frac{1}{PRF}}{\eta_{\text{aperture}}}\right)\exp\left(-2\pi j\frac{R_P\left(\eta - i\frac{1}{PRF}\right)}{\lambda}\right)\end{aligned} \quad . \tag{19}$$

Both chirp and Fourier matrices are Toeplitz and are highly structured. The orthogonality of the vectors in the Fourier matrix is guaranteed since they are all complex-valued harmonics whereas, in the case of the chirp-based matrix, this property strongly depends on the explored bandwidth. This assumption holds for a wide azimuth frequency span as is the case of a multiaperture acquisition. Since we assume the scene is sparse in the space domain, $\mathbf{\Phi}$ is a partial identity matrix.

IV. Multiaperture Exploration

In this section, we summarize some methods suitable for solving the problem of harnessing sparse multiaperture intervals for SAR image formation and we give the details of the proposed CS with Ψ^{CHIRP} workflow presented in Fig. 4. In the following CS-CHIRP and CS-FFT refer to solvers used for the proposed problem based on CS with linear frequency modulated basis vector and Fourier dictionary, respectively.

A. Autoregressive Model

A common method for filling the gaps in audio signals is by using autoregressive (AR) models [53]. However, there are some constraints imposed on the extend of the "gap" under reconstruction [54]. AR models can be employed in the multiaperture processing chain for azimuth profile recovery. Note that AR will fail for large reconstruction intervals since the short-term stationarity assumption is no longer verified. For the sake of comparison, we use Forward-Backward trained AR models. In plain terms, the missing samples are extrapolated from both existing sets of points surrounding the gap. The AR model order selection is given by the Akaike information criteria [55].

B. CS-FFT

A simple CS-based way for solving our problem is to consider the assumption of spatial sparsity and to use the Fourier basis as a sparsifying dictionary. Although this approach significantly reduces the computational complexity it faces the following issue: for large integration intervals, the extremely narrow band assumption on cross-range direction fails. Moreover, it is more sensitive to noise than the CHIRP-based method.

C. Proposed Processing: CS-CHIRP

The main goal of this article is to derive a CS-based scheme for azimuth profile reconstruction, such that the multiple-aperture available data contribute to azimuth resolution enhancement. We evaluate two CS-based approaches and the AR-based recovery technique. Before casting the data to one of those frameworks, the signals from the two receiving channels data are preprocessed. Thus, the following operations are performed: azimuth antenna pattern (AAP) compensation, range compression as discussed in Section II and azimuth resampling. AAP compensation may be easily merged into the general CS frame but it needs to be carefully performed since TOPS mode introduces a range-dependent Doppler centroid shift caused by steering of the transmitter antenna beam. The last procedure is needed as a consequence of different pulse repetition frequencies used in the TOPS mode for each subswath. Next, the KT transform [22] is applied for linear RCM removal. Since range and azimuth have been decoupled, the reconstruction algorithm may be applied independently on each iso-range. The proposed workflow reramps the range compressed data, then constructs the CHIRP sparsifying dictionary according to the azimuth extent of the multiaperture interval and a specific mid-range swath using (19). After a large-scale suitable CS solver algorithm is applied, the reconstructed data is deramped. In order to generate the final SAR image by BP algorithm [27], the inverse KT restores the initial linear range walk.

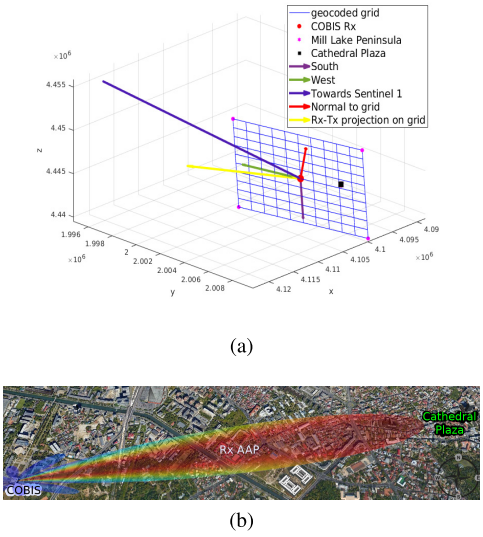

(a)

(b)

Fig. 5. Aligned hyperbola scenario (*Study Case 1*)-corresponding to an ascending orbit of Sentinel-1. (a) Acquisition geometry. (b) Google Earth optical image of the covered area (Bucharest, Romania).

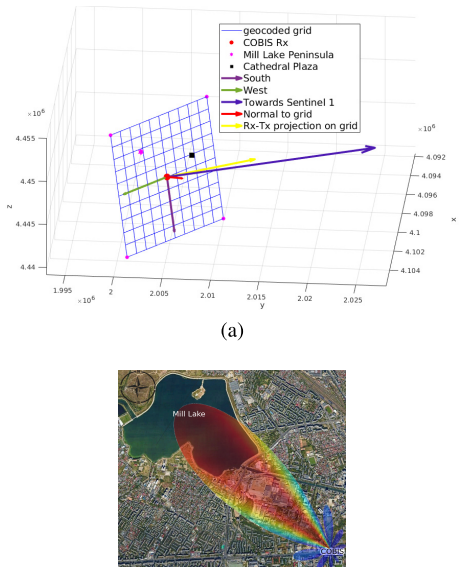

(a)

(b)

Fig. 6. Miss-aligned hyperbola scenario (*Study Case 2*)-corresponding to an ascending orbit of Sentinel-1. (a) Acquisition geometry. (b) Google Earth optical image of the covered area containing the Mill Lake.

D. Computational Complexity

The computational complexity of the proposed multiaperture gap reconstruction framework is given by two KT transforms, two Hadamard multiplications, and the computational complexity of the CS solver. For most of the greedy solvers (e.g., OMP, ROMP, GOMP, CoSaMP, SP), since $K \ll M < N$ the computational amount is $\mathcal{O}(KMN)$. That is because the correlations between the residues and the dictionary atoms are the most resource-consuming operations. Because of its "brute-force" manner of refining the solution, SWAP is one of the least computational effective solvers. Unlike Matching Pursuit approaches, the algorithms based on convex/nonconvex relaxations are more computationally demanding. Among the ones analyzed in this work, the fastest are SPGL1-BPDN and IJT-$L_{2/3}$. Further, the reramping and deramping processes are characterized by $\mathcal{O}(N^2)$. The KT transform implies applying the Fourier Transform over the range direction, $\mathcal{O}(N_s \log(N_s))$, where N_s is the number of range samples. For regular SAR system parameters, $N_s \ll N$. Finally, the linear interpolation step may be efficiently computed with complexity $\mathcal{O}(N^2)$.

V. Experiments and Validation

In this section, we assess the validation of the proposed processing flow. First, simulated data are fed to the workflow in order to evaluate the reconstruction accuracy of the "chopped" azimuth profile. Then, two real-world data sets are processed with the proposed framework. The first represents the particular case in which the hyperbolic phase history corresponding to the receiver synchronization channel (Rx-Tx range) and the Tx-target-Rx semimonostatic hyperbola are azimuth time-aligned. Such an acquisition scenario is sketched in Fig. 5. In other words, the projection of the Tx-Rx line segment onto the Geo-referenced grid is approximately colinear with the receiver LOS (the velocity vector of Sentinel-1 is orthogonal to the Rx LOS). The acquisition setup is configured as follows: COBIS is located on the rooftop of the University "Politehnica" of Bucharest (UPB) central building in Bucharest having its receiving echo channel oriented toward Cathedral Plaza [see Fig. 5(b)]. In Fig. 6, the second real-world data set acquisition setup is shown. This presents a more general case in which the hyperbolic phase from the receiver synchronization channel is no longer aligned with the phase of the illuminated targets. That is why for this case a special range dependent AAP compensation processing is applied. COBIS is located on Building B of the UPB campus and the echo channel is oriented toward Mill Lake, Bucharest [see Fig. 6(b)]. Generally, the hyperparameters of the CS solvers ensure both convergence and estimation accuracy [56]. Thus, for the real-world numerical experiments, they are tuned to offer the best estimate. The greedy solvers halt when the residue decreases under 10% from the initial energy. Concerning the simulated data tests, we have used the real sparsity degree as input for the greedy solvers whereas for the convex/nonconvex solvers the maximum number of iterations was limited to 100. The acquisition scenarios displayed in Figs. 5 and 6 ensure an obtuse angle formed by Sentinel-1-COBIS-area of interest. Hence, the reference channel is the first to receive the transmitted signal, then depending on its energy, the echo channels are triggered.

A. Empirical Imaging Scene Extent

The LFM basis proposed for the CS frame is determined usually according to the scene center and it ensures the level of sparseness for targets in the neighborhood of the reference point. Therefore, we carry out an empirical analysis regarding the scene extent for which the sparsity assumption holds with no upgrade of $\mathbf{\Psi}$. In this sense, only the azimuth chirp slope has been analyzed. Fig. 7 reveals that for the two scenes centered on Mill Lake Peninsula(Bucharest) and Cathedral Plaza (Bucharest) containing an area of 1 km^2, the azimuth frequency slope varies with less than 0.045% for a multiaperture interval of 1.6805 s. However, for larger scene

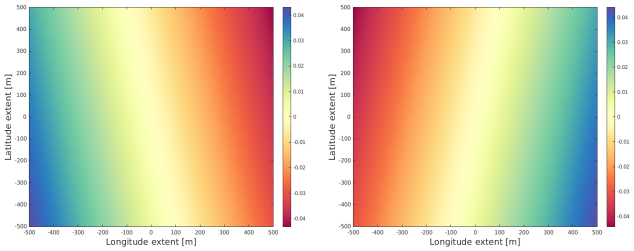

(a) (b)

Fig. 7. Azimuth frequency slope variation on (a) Study case 1 and (b) Study case 2.

extents or for higher reconstruction accuracy, this parameter should be accordingly updated.

B. Simulated Bistatic Data

In this section, we present the performance comparison of different reconstruction methods. More precisely, the proposed processing flow is adapted also for CS recovery with FFT sparsifying basis. The solvers presented in Section III-B are then employed. Apart from CS-based recovery, we also evaluate the AR-based method. Simulations are performed using real-world scenario parameters. Some of the parameters involved are given in Table I. More precisely, the ones corresponding to the second real-world experiment because it explores the case with the biggest degree of generality.

The accuracy parameters presented in Fig. 8 were obtained by considering a single point scatterer i.e., the system point spread function (PSF) and SNR $=$ 3 dB. The following quality parameters were evaluated: the root mean square error (RMSE), the mean absolute phase error (MAPE), the peak-to-sidelobe ratio (PSLR), and the integrated to sidelobes ratio (ISLR). For the results displayed in Fig. 8(a), and Fig. 8(b) represents the gaps in the aperture emulating the ones in the second study case representing $\approx 40\%$ of all samples, and the accuracy variation is strictly dictated by the various noise samples generated over 100 iterations. Before reconstruction, we have altered the ideal signal with white Gaussian noise with SNR $=$ 3 dB. The mean (thick bars) and the standard deviations (thin segments) of the quality parameters are displayed. In Fig. 8(a) and (b), we have also tested the robustness of the recovery against gaps sizes and positions. Thus, we have randomly generated seven gaps representing 30% to 50% of the entire data over 250 trials. Remarkably, that the solvers based on convex relaxations are generally more sensitive to noise (IRLS is the most noise-dependent). A smaller SNR value would drastically decrease their reconstruction accuracy. Except for IRLS, all CS recoveries based on $\mathbf{\Psi}^{\text{CHIRP}}$ outperform AR and CS-FFT. In contrast, the FFT-based reconstructions using greedy approaches fail since we have employed the real sparsity level i.e., $K = 1$ and this assumption is not satisfied for the representation of extended-aperture data in the Fourier domain. In Fig. 8(a) and (b) the most accurate results are provided by the greedy solvers. SPGL-BPDN fails under poor prior noise level estimation. Yet SPGL1-BPDN together with IJT-$L_{2/3}$ are suitable for large-scale problems due to their sped-up convergence. By simultaneously considering RMSE, MAPE, PSLR and, ISLR, the best recovery is obtained by IJT-$L_{2/3}$. The subunitary norm promotes the sparsity more than the L_1 norm whereas the jumping thresholding functions make this algorithm act in a quasi-greedy manner. However for larger noise levels IJT-$L_{2/3}$ also fails. Remarkably, CoSaMP manages to generate a reliable outcome. However, compared to the other greedy solvers, CoSaMP is more sensitive to the sparsity degree miss-estimation, and also it is less efficient when the CS framework employs a redundant dictionary as may be the case of smaller aperture extents.

TABLE I
SIMULATION AND REAL WORLD DATA PARAMETERS

Parameter	Value/Description
F_c	5.405 GHz
F_s	250 MHz (Study case 1), 122.88 MHz (Study case 2)
BW	50 MHz
PRF	2 KHz (after resampling)

For the experiments with real-world data, we will mainly focus on the results provided by the highlighted approaches. If some other algorithm provides a remarkable result, it will be also discussed.

C. Real World Bistatic Data

In this section, we assess an extensive analysis regarding the benefits of the proposed CS recovery against the raw integration, AR and, CS-FFT.

1) Study Case I: For this study case, the receiver echo antenna is oriented toward the east [see Fig. 5(b)]. The bistatic SAR images in Fig. 9 illustrate an urban area of 950 m $\times$ 2350 m from Bucharest, Romania. In Fig. 9(a) the focused SAR image is obtained from a single aperture interval (0.323 s). The raw integration of the multiaperture interval (1.7905 s) is shown in Fig. 9(b). The SAR images resulted after reconstruction of the azimuth profiles are presented in Fig. 9(c)–(i). All methods manage to reduce the effect of the grating lobes. Yet some important observations should be highlighted: CS-FFT methods fail (strong scatterers' main lobes are smeared in the azimuth direction) even though it seems to generate a "clean" SAR image. Generally, the CS-CHIRP methods outperform CS-FFT and AR reconstructions. To prove this, not only by visual inspection, further local analysis is carried on. The area under test is marked with a red rectangle in Fig. 9(a) (200 m $\times$ 200 m). It represents a spatial sparse area containing some strong point scatterers from Cathedral Plaza Tower. First, the proposed processing chain is evaluated by introducing two artificial gaps in the single aperture interval. The gaps have equal lengths and are centered at one quarter and three quarters in the aperture emulating a likely multiaperture real data. We have employed 646 range profiles (0.323 s) and at each of the ten iterations, 50 of them were removed, corresponding to 0.025 s. Therefore, the tenth iteration considers two gaps of 0.125 s each. The remaining data were fed to the reconstruction algorithms. In Fig. 10(a) and (b) are displayed the RMSE of the magnitude component and the recovered phase of the most intense scatterer relative to the SAR image focused using the entire single aperture interval.

Out of the CS-FFT-based approaches, FISTA provides the most accurate result. However, FISTA-$\mathbf{\Psi}^{\text{FFT}}$ does not even

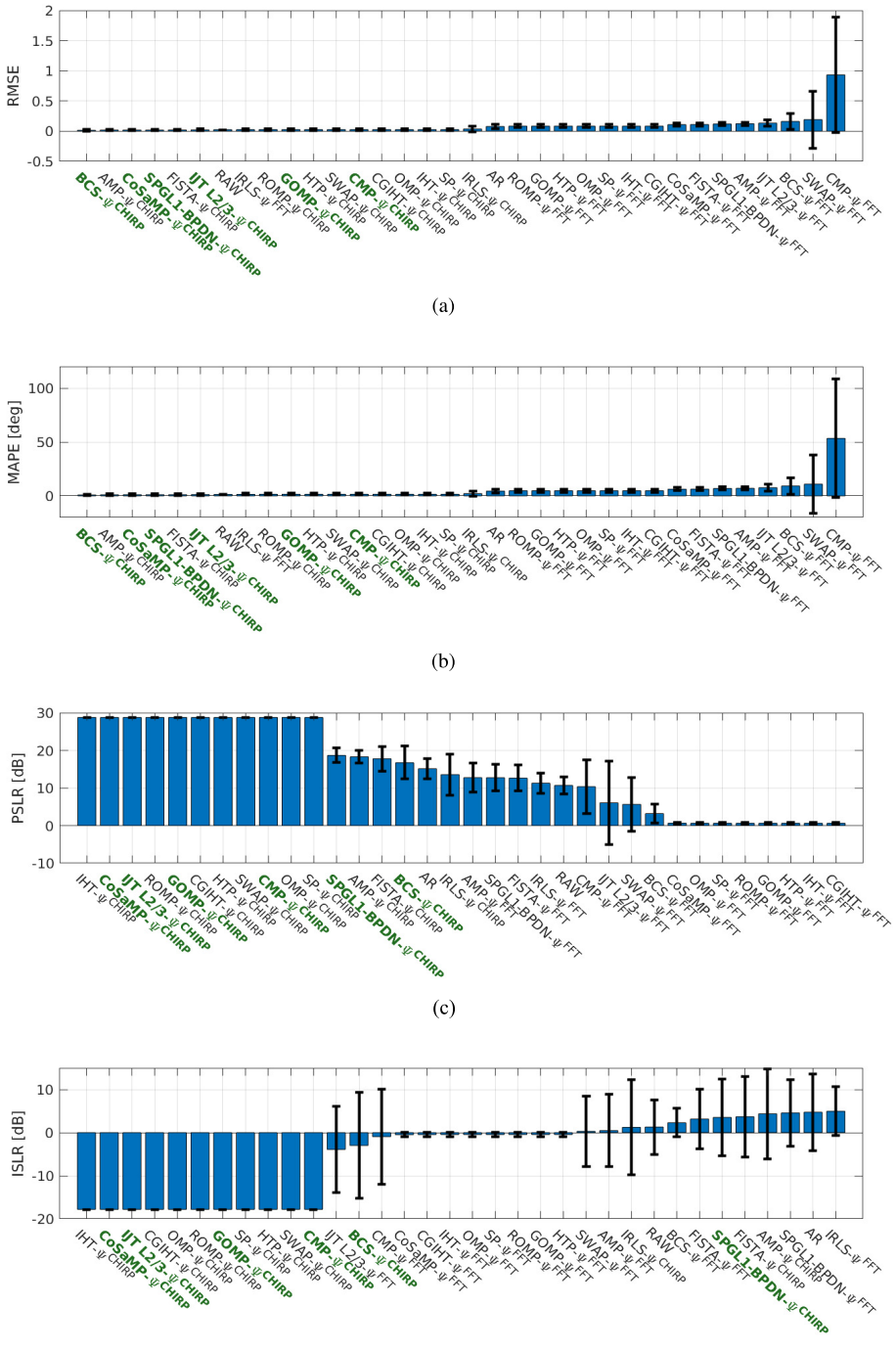

Fig. 8. Reconstruction accuracy on simulated data obtained by various CS solvers using either $\mathbf{\Psi}^{\text{FFT}}$ or $\mathbf{\Psi}^{\text{CHIRP}}$. (a) RMSE. (b) MAPE. (c) PSLR. (d) ISLR. The values are sorted such that the reconstruction accuracy decreases. Each category of solvers has at least one representative approach in the list of highlighted algorithms.

outperform the raw integration. In the CS-CHIRP category, the greedy solvers prove a quasi-invariant response to the gap size. IJT-$L_{2/3}$ performance linearly decreases with respect to the extent of gaps whereas for AR and ROMP, the RMSE increases exponentially. Since the single aperture interval has a high SNR the SPGL1-BPDN has high efficiency in reconstructing the azimuth profiles (both magnitude and phase).

Furthermore, we evaluate the behavior of the recovery algorithms over a multiaperture interval of 1.7905 s (3581 range profiles). The gaps in this interval correspond to critically low SNR (regions centered on the null points in the AAP). All the gaps represent 24.46% from the entire data. The location of the removed profiles can be identified in Fig. 11(a) (dark blue stripes). Some examples of reconstructed azimuth profile results for the region centered on Cathedral Plaza are displayed in Fig. 11(b)–(h).

The greedy solvers provide similar reconstructions whereas some of the convex/nonconvex solvers fail either because the SNR is too low or because the gaps are too large. In Fig. 11(b) the AR results highlight its limitation as the largest gap

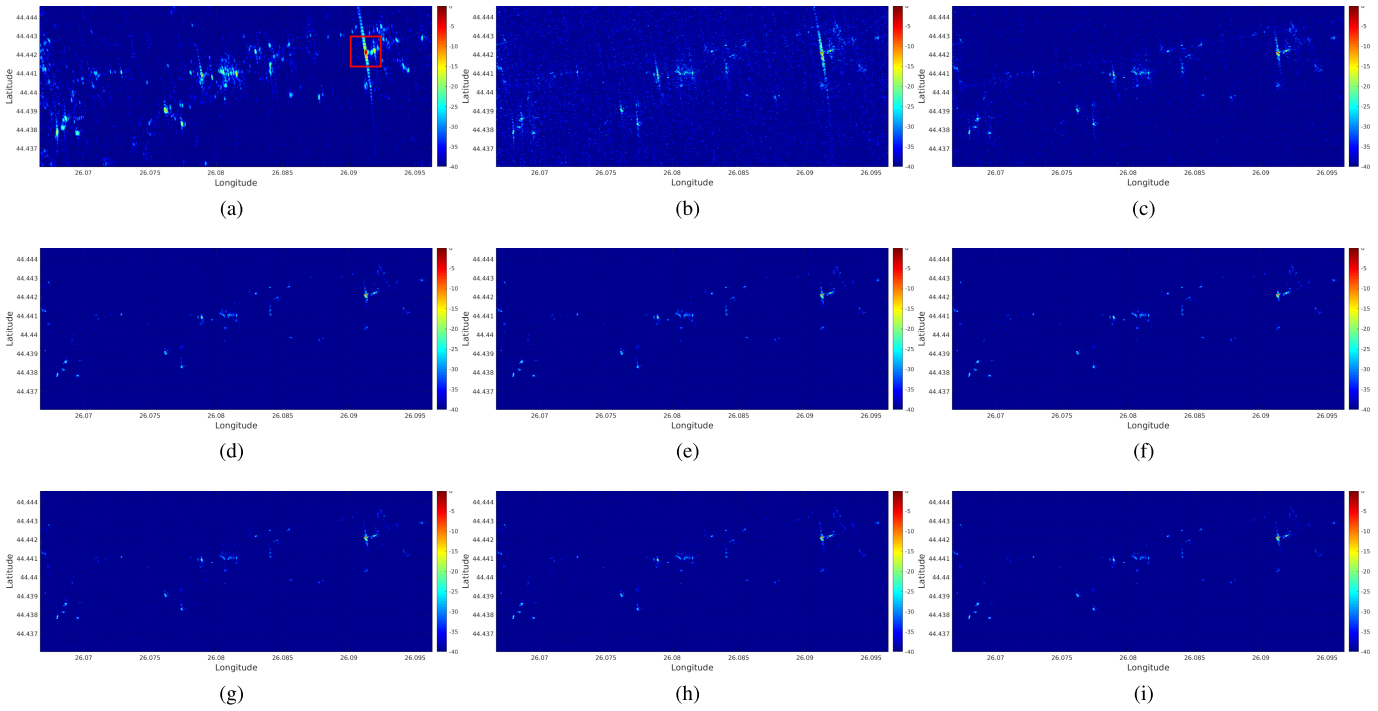

Fig. 9. Extended scene imaging results. (a) Single aperture. (b) Multiaperture raw integration. (c) AR. (d) GOMP-Ψ^{CHIRP}. (e) CoSaMP-Ψ^{CHIRP}. (f) SWAP-Ψ^{CHIRP}. (g) IJT-$L_{2/3}$-Ψ^{CHIRP}. (h) SPGL1-BPDN-Ψ^{CHIRP}. (i) FISTA-Ψ^{FFT}. The CS-CHIRP approaches used adaptive dictionary.

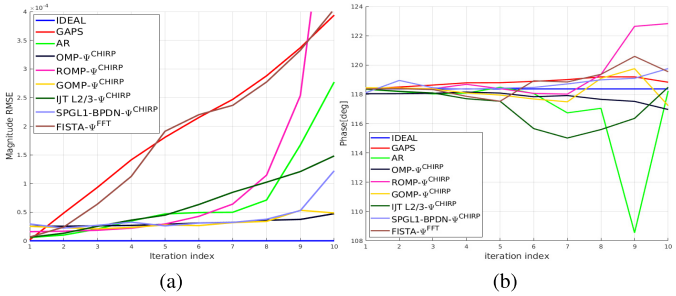

Fig. 10. Quality parameters evaluation on single aperture interval with increasing artificial gaps (Study Case 1). (a) Magnitude RMSE. (b) Reconstructed phase of the most powerful scatterer [center Fig. 12(a)].

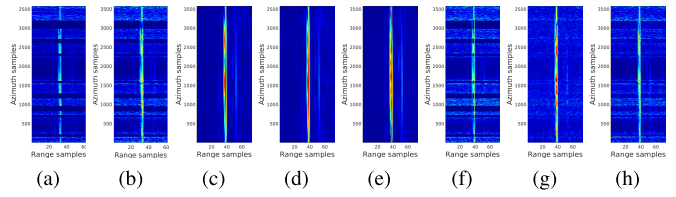

Fig. 11. Azimuth profile reconstruction highlighted on range compressed date centered on Cathedral Plaza. (a) Raw data. (b) AR. (c) CoSaMP-Ψ^{CHIRP}. (d) GOMP-Ψ^{CHIRP}. (e) CMP-Ψ^{CHIRP}. (f) IRLS-Ψ^{CHIRP}. (g) IJT-$L_{2/3}$-Ψ^{CHIRP}. (h) SPGL1-BPDN-Ψ^{CHIRP}.

is partially recovered. In perturbed scenarios, IJT-$L_{2/3}$ and SPGL1-BPDN may amplify the noise as shown in Fig. 11(g) whereas the recovery achieved by IRLS displayed in Fig. 11(f) proves it is unsuitable for noisy cases. Fig. 11 indicates that the range migration over the entire multiaperture interval is extremely small. However, the RCMC step is compulsory otherwise, artifacts may appear in the final SAR image.

The noisy aspect of the naive integration Fig. 12(b) is suppressed by all the greedy methods. Nevertheless, our proposed workflow is superior to AR and CS-FFT in both

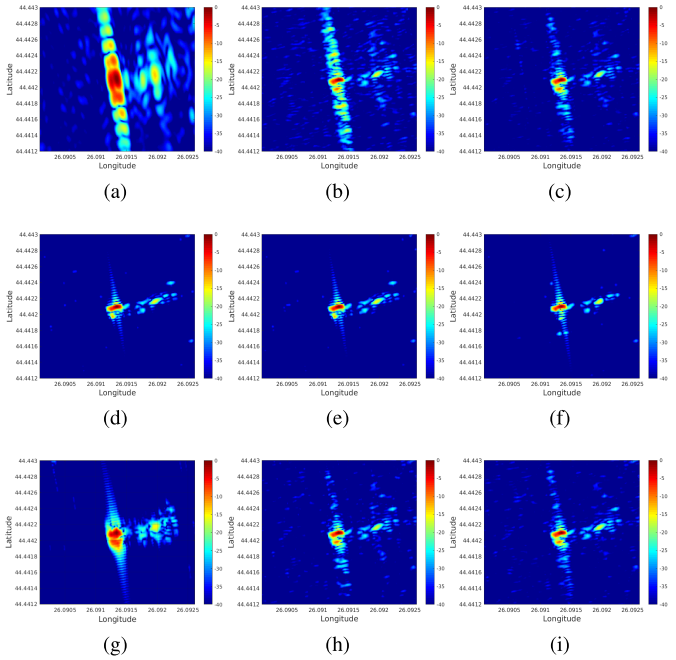

Fig. 12. Normalized bistatic SAR images (in dB [-40,0]) over the patch centered on Cathedral Plaza. (a) Single aperture. (b) Raw data integration. (c) AR. (d) CoSaMP-Ψ^{CHIRP}. (e) GOMP-Ψ^{CHIRP}. (f) CMP-Ψ^{CHIRP}. (g) GOMP-Ψ^{FFT}. (h) IJT-$L_{2/3}$-Ψ^{CHIRP}. (i) SPGL1-BPDN-Ψ^{CHIRP}.

resolution enhancement and grating lobes suppression. The outcomes provided by AR, SPGL1-BPDN, and IJT-$L_{2/3}$ shown in Fig. 12(c), Fig. 11(h), and Fig. 12(h) partially mitigate the sidelobes because the largest gaps are erroneously reconstructed. On the other side, CoSaMP, GOMP, and CMP [Fig. 12(d)–(f)] may achieve high-quality reconstructions over sparse scenes confirming their robustness to noise and gap extend.

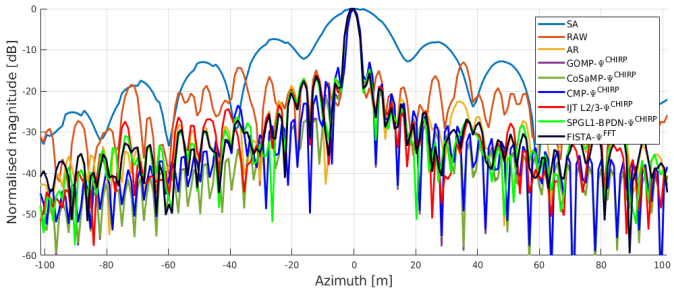

Fig. 13. Azimuth sections crossing the strongest point-scatterer in the SAR images shown in Fig. 12.

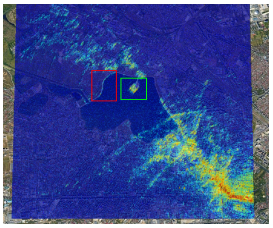

Fig. 14. Multiaperture focusing overlaying Google Earth optical image. Sparse areas are marked by red (Mill Lake dam) and green (Mill Lake peninsula) frames.

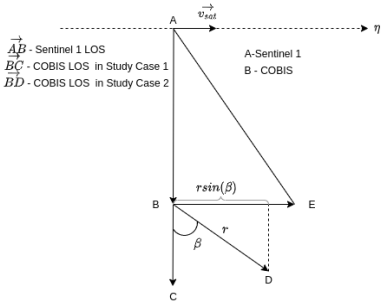

Fig. 15. Simplified acquisition geometry in geocoded grid coordinates.

Fig. 13 presents the normalized cross-range sections (in dB) over the most powerful scatterer in the SAR images in Fig. 12. The undesired sidelobe influence is reduced by the CS-based processing flow. By harnessing a multiaperture interval, the azimuth resolution at -3 dB is enhanced from $\approx$16 m to $\approx$3.25 m. However, the overall SAR image aspect is strongly influenced by the presence of the grating lobes. The best sidelobes suppression is achieved by CoSaMP, GOMP and, OMP with $\boldsymbol{\Psi}^{\text{CHIRP}}$. The average azimuth grating lobes mitigation is $\approx$14.90 dB relative to the SAR image obtained by raw integration. AR achieves a sidelobe reduction with $\approx$6.9 dB. The CS-FFT greedy methods fail for large integration intervals as displayed in Fig. 12(g). This happens because, for an aperture length of 1.7905 s, the resulted azimuth band of the range compressed data is $\approx$3.9 Hz. This small azimuth bandwidth gathers eight frequency bins, thus, the sparsity approximation in the Fourier domain is no longer sustained (does not match the number of the point scatterers in the scene). Nevertheless, since the nongreedy approaches do not need an estimate of the sparsity degree, they manage to provide more accurate results with FFT sparsifying dictionary (FISTA-$\boldsymbol{\Psi}^{\text{FFT}}$ section in Fig. 13).

2) Study Case II: The sketch in Fig. 6 shows the acquisition scenario for this study case. The receiver, located at

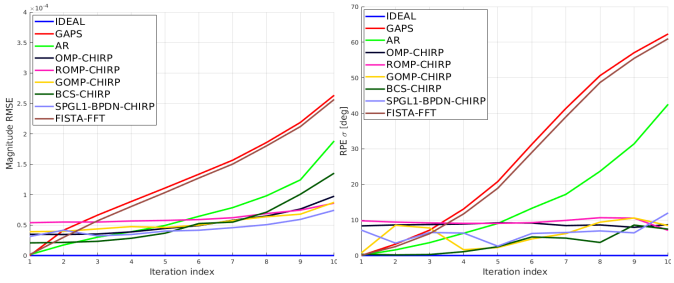

(a) (b)

Fig. 16. Quality parameters evaluation for second study case. (a) RMSE. (b) RPE standard deviation.

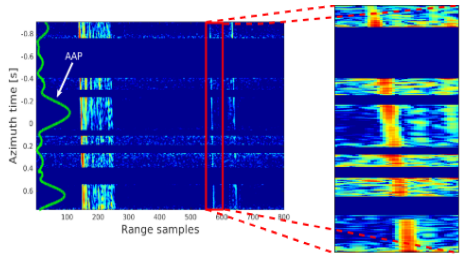

Fig. 17. Range compressed image corresponding to second study case illustrating reflected signal from Mill Lake peninsula and Mill Lake dam. The zoomed area indicates the linear range walk of a strong scatterer.

[44.434063 N, 26.057119 E] has the echo channel main lobe antenna oriented toward Mill Lake in Bucharest, Romania. Unlike the first case, the Rx LOS is no more collinear with the Rx-Tx segment. As illustrated in Fig. 17, for this case the range cell migration step is essential before the gap-filling processing block. Another significant difference to the previous case is that the spatial sparsity assumption in the ambiguity-free region is valid for fewer regions. As marked in Fig. 14, only two areas in the neighborhood of the water body will be considered in the following experiments: Mill Lake dam (red frame) and Mill Lake peninsula (green frame). Data were recorded on the 7th of March 2020. Another particularity of this second study case is given by the AAP compensation step. For each iso-range line, an updated version of the AAP should be considered. The AAP linear shift in (20) over range may be easily estimated from the misalignment shown in Figs. 6 and 15. Specifically, the AAP shift slope is given by the angle between the Rx LOS and Rx-Tx segment projection on the focusing grid (β). Before considering a multiaperture interval we assess the same procedure of introducing two synthetic gaps in the single aperture interval. The quality parameters displayed in Fig. 16 were obtained by using the main lobe pulses interval (0.35 s) and introducing two equal gaps. The gaps were progressively enlarged by 0.0125 s each over 10 iterations. The patch under test contains the Mill Lake Peninsula (green frame in Fig. 14) and covers an area of 500 m $\times$ 500 m

$$\text{AAP}_D(\eta) \approx \text{AAP}_B\left(\eta - \frac{r\sin(\beta)}{|\vec{v}_{\text{sat}}|}\right). \tag{20}$$

The performance parameters displayed in Fig. 16 confirm that CS-CHIRP methods surpass AR and CS-FFT for larger gaps in terms of RMSE for magnitude and relative phase error (RPE) standard deviation.

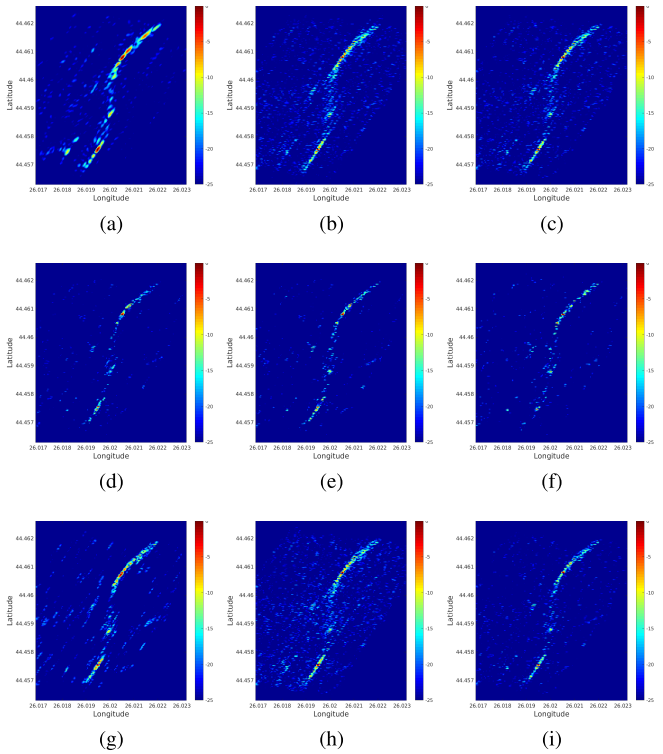

Fig. 18. Normalized bistatic SAR images (in dB [-25,0]) over the patch centered on Mill Lake Dam (red frame). (a) Single aperture. (b) Raw data integration. (c) AR. (d) CoSaMP-Ψ^{CHIRP}. (e) GOMP-Ψ^{CHIRP}. (f) CMP-Ψ^{CHIRP}. (g) GOMP-Ψ^{FFT}. (h) IJT-$L_{2/3}$. (i) SPGL1-BPDN-Ψ^{CHIRP}.

The CS-FFT reconstructions produced by the greedy solvers reveal an unstable behavior. Except for CoSaMP and CGIHT, all the greedy algorithms manage to achieve performances similar to OMP, ROMP, and GOMP. The methods based on belief propagation, i.e., BCS and AMP, in conjunction with the CHIRP dictionary offer a precise recovery of the signal for relatively small gaps. Using the FFT dictionary, the CS-solvers do not obtain good enough results. The most competitive result is provided by FISTA.

The two subregions marked in Fig. 14 are separately analyzed for a multiaperture interval of 1.68 s. A part of the range compressed for this study case is illustrated in Fig. 17. The zoomed area stresses the considerable linear range walk whereas, in the left part, the AAP overlays the "chopped" data. It worth noticing that the biggest gap lasts 0.4 s, almost twice bigger than the largest gap in the *Study Case I*.

The first evaluated region presents the dam in the northwest of Mill Lake. The area (700 m $\times$ 500 m) is centered on [44.45945 N, 26.02005E]. In Fig. 18(c) the outcome provided after AR reconstruction shows that it just manages to slightly reduce the grating lobes. In contrast, the greedy CS-CHIRP approaches [Fig. 18(d)–(f)] manage to enhance the resolution, to preserve the "S" shape of the dam together with an important attenuation of the sidelobes. The failure of CS-FFT is emphasized in Fig. 18(g).

The second image covers a 500 m $\times$ 500 m area and is centered on [44.45881 N, 26.02909 E]. Initially, the sidelobes corresponding to the scatterers from the Mill Lake peninsula cover a significant part of the water-body. Even though for the structural part of the dam the failure of the CS-FFT method is

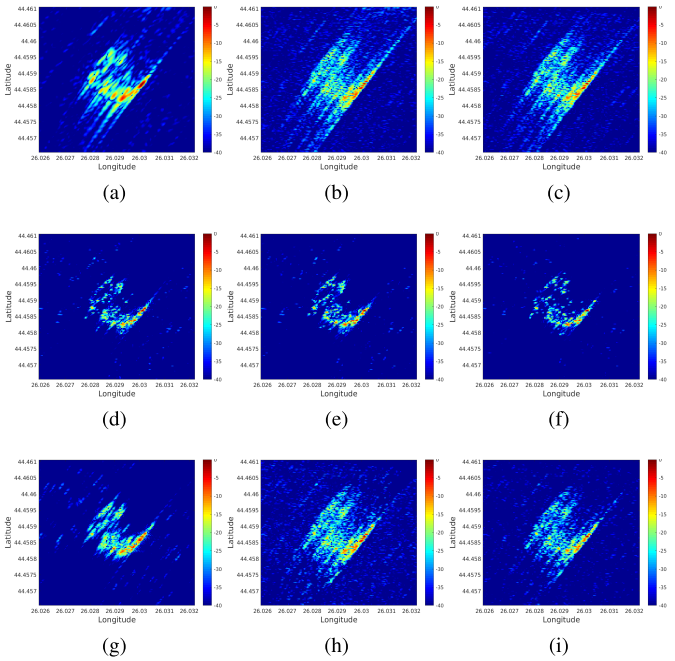

Fig. 19. Normalized bistatic SAR images (in dB [-40, 0]) over the patch centered on Mill Lake Peninsula (green frame). (a) Single aperture. (b) Raw data integration. (c) AR. (d) CoSaMP-Ψ^{CHIRP}. (e) GOMP-Ψ^{CHIRP}. (f) CMP-Ψ^{CHIRP}. (g) GOMP-Ψ^{FFT}. (h) IJT-$L_{2/3}$-Ψ^{CHIRP}. (i) SPGL1-BPDN-Ψ^{CHIRP}.

not so obvious, in Fig. 19(g) it may be noticed that the SAR image seems defocused. This artifact is produced by the poor approximation of the azimuth narrow band in the context of a large integration interval.

AR does not manage to reconstruct the bistatic azimuth profiles corresponding to the Mill Lake Peninsula. In addition, not even CS-CHIRP methods [Fig. 19(h) and (i)] based on convex/nonconvex solvers do not achieve a great performance in reducing the sidelobes. The accuracy is low because the proportion of available data and also the SNR is smaller than that in the context of the *Study Case I*. Even though the greedy solvers may provide qualitative reconstructions [Fig. 19(d)–(f)] they are more sensitive to AAP compensation error than other categories of CS solvers. This lack of robustness is caused by the residue update step which is performed by subtracting the contribution of the very last selected dictionary atom(s).

VI. Conclusion

This article presented a CS-based methodology for resolution enhancement in the context of an opportunistic bistatic SAR imaging having Sentinel-1 as a transmitter and COBIS as a ground-based receiver. The use of the CS concept for signal reconstruction is essentially based on spatial sparsity assumption on each iso-range and the existence of a chirp-based sparsifying dictionary. The framework exploits the opportunistic acquisition properties of the data. First, low complexity and effective RCMC algorithm (KT) is employed and then the azimuth band is expanded using Sentinel-1 orbital parameters. Furthermore, we choose to remove the range profiles with low SNR and recover the missing azimuth samples by various CS solvers in conjunction with a locally adapted chirp-based sparsifying basis. An extensive list of greedy, convex and,

nonconvex relaxation algorithms was discussed and compared. The experimental results over diverse acquisition scenarios demonstrate the effectiveness of the proposed method regarding the following two aspects: cross-range resolution improvement and grating lobes suppression.CS-CHIRP approaches outperform the AR model and CS-FFT in terms of amplitude RMSE and phase error. Moreover, as opposed to CS-FFT which is strongly influenced by the length of the synthetic aperture, AR which is pushed to the limit of its working interval (50 ms), the proposed workflow proved to be quasi-invariant to extent of the gaps.

REFERENCES

[1] O. Loffeld, H. Nies, V. Peters, and S. Knedlik, "Models and useful relations for bistatic SAR processing," *IEEE Trans. Geosci. Remote Sens.*, vol. 42, no. 10, pp. 2031–2038, Oct. 2004.

[2] I. Walterscheid, J. H. G. Ender, A. R. Brenner, and O. Loffeld, "Bistatic SAR processing and experiments," *IEEE Trans. Geosci. Remote Sens.*, vol. 44, no. 10, pp. 2710–2717, Oct. 2006.

[3] J. Sanz-Marcos, P. Lopez-Dekker, J. J. Mallorqui, A. Aguasca, and P. Prats, "SABRINA: A SAR bistatic receiver for interferometric applications," *IEEE Geosci. Remote Sens. Lett.*, vol. 4, no. 2, pp. 307–311, Apr. 2007.

[4] F. Behner, S. Reuter, H. Nies, and O. Loffeld, "Synchronization and processing in the HITCHHIKER bistatic SAR experiment," *IEEE J. Sel. Topics Appl. Earth Observ. Remote Sens.*, vol. 9, no. 3, pp. 1028–1035, Mar. 2016.

[5] A. Anghel, R. Cacoveanu, A.-S. Moldovan, B. Rommen, and M. Datcu, "COBIS: Opportunistic C-band bistatic SAR differential interferometry," *IEEE J. Sel. Topics Appl. Earth Observ. Remote Sens.*, vol. 12, no. 10, pp. 3980–3998, Oct. 2019.

[6] V. Kubica, X. Neyt, and H. Griffiths, "Along-track resolution enhancement for bistatic imaging in burst-mode operation," *IEEE Trans. Aerosp. Electron. Syst.*, vol. 52, no. 4, pp. 1568–1575, Aug. 2016.

[7] A. Anghel, R. Cacoveanu, B. Rommen, and M. Datcu, "Multi-aperture focusing in spaceborne transmitter-stationary receiver bistatic SAR," in *Proc. IEEE Int. Geosci. Remote Sens. Symp. (IGARSS)*, Jul. 2019, pp. 1120–1123.

[8] P. Lopez-Dekker, J. J. Mallorqui, P. Serra-Morales, and J. Sanz-Marcos, "Phase synchronization and Doppler centroid estimation in fixed receiver bistatic SAR systems," *IEEE Trans. Geosci. Remote Sens.*, vol. 46, no. 11, pp. 3459–3471, Nov. 2008.

[9] H. Zhang *et al.*, "Spaceborne/Stationary bistatic SAR imaging with TerraSAR-X as an illuminator in staring-spotlight mode," *IEEE Trans. Geosci. Remote Sens.*, vol. 54, no. 9, pp. 5203–5216, Sep. 2016.

[10] I. Walterscheid *et al.*, "Bistatic SAR experiments with PAMIR and TerraSAR-X—Setup, processing, and image results," *IEEE Trans. Geosci. Remote Sens.*, vol. 48, no. 8, pp. 3268–3279, Aug. 2010.

[11] F. De Zan and A. Monti Guarnieri, "TOPSAR: Terrain observation by progressive scans," *IEEE Trans. Geosci. Remote Sens.*, vol. 44, no. 9, pp. 2352–2360, Sep. 2006.

[12] A. Focsa, M. Datcu, and A. Anghel, "Compressed sensing-based multi-aperture focusing of spaceborne transmitter/stationary receiver bistatic SAR data," in *Proc. IEEE Radar Conf. (RadarConf)*, Sep. 2020, pp. 1–4.

[13] R. Baraniuk and P. Steeghs, "Compressive radar imaging," in *Proc. IEEE Radar Conf.*, Apr. 2007, pp. 128–133.

[14] A. De Maio, Y. C. Eldar, and A. M. Haimovich, *Compressed Sensing in Radar Signal Processing*. Cambridge, U.K.: Cambridge Univ. Press, 2019.

[15] C. J. Della Porta, A. A. Bekit, B. H. Lampe, and C.-I. Chang, "Hyperspectral image classification via compressive sensing," *IEEE Trans. Geosci. Remote Sens.*, vol. 57, no. 10, pp. 8290–8303, Oct. 2019.

[16] M. Cetin *et al.*, "Sparsity-driven synthetic aperture radar imaging: Reconstruction, autofocusing, moving targets, and compressed sensing," *IEEE Signal Process. Mag.*, vol. 31, no. 4, pp. 27–40, Jul. 2014.

[17] I. Stojanovic, M. Cetin, and W. C. Karl, "Compressed sensing of monostatic and multistatic SAR," *IEEE Geosci. Remote Sens. Lett.*, vol. 10, no. 6, pp. 1444–1448, Nov. 2013.

[18] M. Tello Alonso, P. Lopez-Dekker, and J. J. Mallorqui, "A novel strategy for radar imaging based on compressive sensing," *IEEE Trans. Geosci. Remote Sens.*, vol. 48, no. 12, pp. 4285–4295, Dec. 2010.

[19] R. Bamler, "A comparison of range-Doppler and wavenumber domain SAR focusing algorithms," *IEEE Trans. Geosci. Remote Sens.*, vol. 30, no. 4, pp. 706–713, Jul. 1992.

[20] M. Y. Jin, F. Cheng, and M. Chen, "Chirp scaling algorithms for SAR processing," in *Proc. IEEE Int. Geosci. Remote Sens. Symp. (IGARSS)*, 1993, pp. 1169–1172.

[21] R. K. Raney, H. Runge, R. Bamler, I. G. Cumming, and F. H. Wong, "Precision SAR processing using chirp scaling," *IEEE Trans. Geosci. Remote Sens.*, vol. 32, no. 4, pp. 786–799, Jul. 1994.

[22] R. P. Perry, R. C. Dipietro, and R. L. Fante, "SAR imaging of moving targets," *IEEE Trans. Aerosp. Electron. Syst.*, vol. 35, no. 1, pp. 188–200, Jan. 1999.

[23] X. Qiu *et al.*, "An imaging algorithm based on keystone transform for one-stationary bistatic SAR of spotlight mode," *EURASIP J. Adv. Signal Process.*, vol. 2012, no. 1, p. 221, Dec. 2012.

[24] Y. Jungang, H. Xiaotao, J. Tian, J. Thompson, and Z. Zhimin, "New approach for SAR imaging of ground moving targets based on a keystone transform," *IEEE Geosci. Remote Sens. Lett.*, vol. 8, no. 4, pp. 829–833, Jul. 2011.

[25] Y. He, P. Aubry, F. Le Chevalier, and A. Yarovoy, "Keystone transform based range-Doppler processing for human target in UWB radar," in *Proc. IEEE Radar Conf.*, May 2014, pp. 1347–1352.

[26] J. Tian, W. Cui, X.-G. Xia, and S.-L. Wu, "Parameter estimation of ground moving targets based on SKT-DLVT processing," *IEEE Trans. Comput. Imag.*, vol. 2, no. 1, pp. 13–26, Mar. 2016.

[27] M. Soumekh, *Synthetic Aperture Radar Signal Processing*, vol. 7. New York, NY, USA: Wiley, 1999.

[28] D. L. Donoho, "Compressed sensing," *IEEE Trans. Inf. Theory*, vol. 52, no. 4, pp. 1289–1306, Apr. 2006.

[29] M. Rani, S. B. Dhok, and R. B. Deshmukh, "A systematic review of compressive sensing: Concepts, implementations and applications," *IEEE Access*, vol. 6, pp. 4875–4894, 2018.

[30] E. Crespo Marques, N. Maciel, L. Naviner, H. Cai, and J. Yang, "A review of sparse recovery algorithms," *IEEE Access*, vol. 7, pp. 1300–1322, 2019.

[31] R. Tibshirani, "Regression shrinkage and selection via the lasso," *J. Roy. Stat. Soc., B (Methodol.)*, vol. 58, no. 1, pp. 267–288, Jan. 1996.

[32] E. Candes and T. Tao, "The dantzig selector: Statistical estimation when p is much larger than n," *Ann. Statist.*, vol. 35, no. 6, pp. 2313–2351, Dec. 2007.

[33] S. S. Chen, D. L. Donoho, and M. A. Saunders, "Atomic decomposition by basis pursuit," *SIAM Rev.*, vol. 43, no. 1, pp. 129–159, Jan. 2001.

[34] J. A. Tropp and A. C. Gilbert, "Signal recovery from random measurements via orthogonal matching pursuit," *IEEE Trans. Inf. Theory*, vol. 53, no. 12, pp. 4655–4666, Dec. 2007.

[35] D. Needell and R. Vershynin, "Signal recovery from incomplete and inaccurate measurements via regularized orthogonal matching pursuit," *IEEE J. Sel. Topics Signal Process.*, vol. 4, no. 2, pp. 310–316, Apr. 2010.

[36] J. Wang, S. Kwon, and B. Shim, "Generalized orthogonal matching pursuit," *IEEE Trans. Signal Process.*, vol. 60, no. 12, pp. 6202–6216, Dec. 2012.

[37] D. Needell and J. A. Tropp, "CoSaMP: Iterative signal recovery from incomplete and inaccurate samples," *Appl. Comput. Harmon. Anal.*, vol. 26, no. 3, pp. 301–321, May 2009.

[38] T. Blumensath and M. E. Davies, "Iterative hard thresholding for compressed sensing," *Appl. Comput. Harmon. Anal.*, vol. 27, no. 3, pp. 265–274, Nov. 2009.

[39] W. Dai and O. Milenkovic, "Subspace pursuit for compressive sensing signal reconstruction," *IEEE Trans. Inf. Theory*, vol. 55, no. 5, pp. 2230–2249, May 2009.

[40] J. D. Blanchard, J. Tanner, and K. Wei, "Cgiht: Conjugate gradient iterative hard thresholding for compressed sensing and matrix completion," *Inf. Inference, J. IMA*, vol. 4, no. 4, pp. 289–327, 2015.

[41] S. Foucart, "Hard thresholding pursuit: An algorithm for compressive sensing," *SIAM J. Numer. Anal.*, vol. 49, no. 6, pp. 2543–2563, Jan. 2011.

[42] D. Vats and R. G. Baraniuk, "Swapping variables for high-dimensional sparse regression with correlated measurements," 2013, *arXiv:1312.1706*. [Online]. Available: http://arxiv.org/abs/1312.1706

[43] Y. Wang, Y. Y. Tang, and L. Li, "Correntropy matching pursuit with application to robust digit and face recognition," *IEEE Trans. Cybern.*, vol. 47, no. 6, pp. 1354–1366, Jun. 2017.

[44] D. L. Donoho, A. Maleki, and A. Montanari, "Message-passing algorithms for compressed sensing," *Proc. Nat. Acad. Sci. USA*, vol. 106, no. 45, pp. 18914–18919, Nov. 2009.

[45] E. van den Berg and M. P. Friedlander. (Dec. 2019). *SPGL1: A Solver for Large-Scale Sparse Reconstruction*. [Online]. Available: https://friedlander.io/spgl1
[46] A. Beck and M. Teboulle, "A fast iterative shrinkage-thresholding algorithm for linear inverse problems," *SIAM J. Imag. Sci.*, vol. 2, no. 1, pp. 183–202, Jan. 2009.
[47] S. Ji, Y. Xue, and L. Carin, "Bayesian compressive sensing," *IEEE Trans. Signal Process.*, vol. 56, no. 6, pp. 2346–2356, Jun. 2008.
[48] R. Chartrand and W. Yin, "Iteratively reweighted algorithms for compressive sensing," in *Proc. IEEE Int. Conf. Acoust., Speech Signal Process.*, Mar. 2008, pp. 3869–3872.
[49] J. Zeng, S. Lin, and Z. Xu, "Sparse regularization: Convergence of iterative jumping thresholding algorithm," *IEEE Trans. Signal Process.*, vol. 64, no. 19, pp. 5106–5118, Oct. 2016.
[50] E. J. Candes, M. B. Wakin, and S. P. Boyd, "Enhancing sparsity by reweighted ℓ_1 minimization," *J. Fourier Anal. Appl.*, vol. 14, nos. 5–6, pp. 877–905, 2008.
[51] I. Daubechies, M. Defrise, and C. De Mol, "An iterative thresholding algorithm for linear inverse problems with a sparsity constraint," *Commun. Pure Appl. Math.*, vol. 57, no. 11, pp. 1413–1457, 2004.
[52] Z. Ben-Haim, Y. C. Eldar, and M. Elad, "Coherence-based performance guarantees for estimating a sparse vector under random noise," *IEEE Trans. Signal Process.*, vol. 58, no. 10, pp. 5030–5043, Oct. 2010.
[53] W. Etter, "Restoration of a discrete-time signal segment by interpolation based on the left-sided and right-sided autoregressive parameters," *IEEE Trans. Signal Process.*, vol. 44, no. 5, pp. 1124–1135, May 1996.
[54] I. Kauppinen and K. Roth, "Audio signal extrapolation–theory and applications," in *Proc. DAFx*, 2002, pp. 105–110.
[55] H. Akaike, "Fitting autoregressive models for prediction," *Ann. Inst. Stat. Math.*, vol. 21, no. 1, pp. 243–247, Dec. 1969.
[56] Y. Wei, Y. Li, Z. Ding, Y. Wang, T. Zeng, and T. Long, "SAR parametric super-resolution image reconstruction methods based on ADMM and deep neural network," *IEEE Trans. Geosci. Remote Sens.*, early access, Jan. 29, 2021, doi: 10.1109/TGRS.2021.3052793.

Adrian Focsa (Student Member, IEEE) received the B.S. degree in electronics and telecommunications from the Military Technical Academy, Bucharest, Romania, in 2016, and the M.S. degree in electronics and telecommunications from Politehnica University Politehnica of Bucharest (UPB), Bucharest, in 2018. He is pursuing the Ph.D. degree in electronics and telecommunications with the Politehnica University of Bucharest.

He joined the CEOSpaceTech Center, UPB, in 2015 when he also worked at German Aerospace Center (DLR), Weßling, Germany, during two months of internship. He took part in several national and international research projects. His areas of interest include synthetic aperture radar, SAR interferometry, compressive sensing, and machine learning.

Andrei Anghel (Senior Member, IEEE) received the Engineering degree (as valedictorian) and the M.S. degree (Hons.) in electronic engineering and telecommunications from the Politehnica of Bucharest (UPB), Bucharest, Romania, in 2010 and 2012, respectively, and the joint Ph.D. degree in signal, image, speech, and telecoms from the University of Grenoble Alpes, Grenoble, France, and the joint Ph.D. degree *(summa cum laude)* in electronic engineering and telecommunications from UPB in 2015. He received the habilitation degree in electronic engineering, telecommunications and information technologies from UPB in 2020.

From 2012 to 2015, he worked as a Doctoral Researcher with the Grenoble Image Speech Signal Automatics Laboratory (GIPSA-lab), Grenoble. In 2012, he joined the University Politehnica of Bucharest as a Teaching Assistant, where he is an Associate Professor with the Department of Telecommunications, Faculty of Electronics, Telecommunications and Information Technology. His research interests include remote sensing, radar, microwaves and signal processing. He has authored more than 50 scientific publications, 2 textbooks, and a book about SAR signal processing for infrastructure monitoring. He regularly acts as a Reviewer for several IEEE and The Institution of Engineering and Technology (IET) journals.

Dr. Anghel was a recipient of two gold medals at the International Physics Olympiads in 2005 and 2006.

Mihai Datcu (Fellow, IEEE) received the M.S. and Ph.D. degrees in electronics and telecommunications from the University Politehnica of Bucharest (UPB), Bucharest, Romania, in 1978 and 1986, respectively, and the habilitation a Diriger Des Recherches degree in computer science from the University Louis Pasteur, Strasbourg, France, in 1999.

Since 1981, he has been a Professor with the Department of Applied Electronics and Information Engineering, Faculty of Electronics, Telecommunications and Information Technology, UPB. Since 1993, he has been a Scientist with the German Aerospace Center (DLR), Weßling, Germany. His research interests include explainable and physics aware Artificial Intelligence (AI), smart radar sensors design, and qauntum machine learning with applications in Earth Observation. He has held a Visiting Professor appointments with the University of Oviedo, Oviedo, Spain, the University Louis Pasteur and the International Space University, both in Strasbourg, France, University of Siegen, Siegen, Germany, University of Innsbruck, Innsbruck, Austria, University of Alcala, Alcala, Spain, University Tor Vergata, Rome, Italy, University of Trento, Italy, Unicamp, Campinas, Brazil, China Academy of Science (CAS), Shenyang, China, Universidad Pontificia de Salamanca, campus de Madrid, Spain, University of Camerino, Camerino, Italy, the Swiss Center for Scientific Computing (CSCS), Manno, Switzerland. From 1992 to 2002, he had an Invited Professor Assignment with the Swiss Federal Institute of Technology (ETH Zurich), Zurich, Switzerland. Since 2001, he has been initiating and leading the Competence Center on Information Extraction and Image Understanding for Earth Observation, Paris Institute of Technology, ParisTech, France, a collaboration of DLR with the French Space Agency (CNES). He has been a Professor holder of the DLR-CNES Chair at ParisTech. He has initiated the European frame of projects for image information mining (IIM) and is involved in research programs for information extraction, data mining and knowledge discovery, and data science with the European Space Agency (ESA), NASA, and in a variety of national and European projects. He is the Director of the Research Center for Spatial Information, UPB. He is a Senior Scientist and the Data Intelligence and Knowledge Discovery Research Group Leader with the Remote Sensing Technology Institute, DLR and delegate in the DLR-ONERA Joint Virtual Center for AI in Aerospace. He is a member of the ESA Working Group Big Data from Space and Visiting Professor withe ESA's Φ-Lab.

Dr. Datcu was a recipient the National Order of Merit with the rank of Knight, for outstanding international research results, awarded by the President of Romania, in 2008, and the Romanian Academy Prize Traian Vuia for the development of the system for automated analysis of digital images (SAADI) analysis system and his activity in image processing in 1987 and of the Chaire d'excellence internationale Blaise Pascal 2017 for international recognition in the field of data science in Earth observation. He has served as a Co-organizer for international conferences and workshops and as a Guest Editor for a special issues on AI and Big Data of the IEEE and other journals. He is the Representative of Romanian in the Earth Observation Program Board (EO-PB).